

# Radiation environment performance of JWST prototype FPAs

M. E. McKelvey\*<sup>a</sup>, K. A. Ennico<sup>a</sup>, R. R. Johnson<sup>a</sup>, P. W. Marshall<sup>d</sup>, R. E. McMurray<sup>a</sup>, Jr., C. R. McCreight<sup>a</sup>, J. C. Pickel<sup>c</sup>, R. A. Reed<sup>b</sup>

<sup>a</sup>NASA Ames Research Center, Moffett Field, CA 94035-1000

<sup>b</sup>NASA Goddard Space Flight Center, Greenbelt, MD 20771

<sup>c</sup>Pickel R&T, Inc., Bonsall, CA 92003

<sup>d</sup>Consultant to GSFC

## ABSTRACT

As the logical extension of the 20-year mission of the Hubble Space Telescope, NASA plans to launch the James Webb Space Telescope (JWST, formerly NGST) near the end of this decade. As Hubble's scientific and technological successor, equipped with a 6-meter-class deployable mirror, JWST will allow observations of the very early universe and initial formation of galaxies at levels not achievable today. JWST's unprecedented sensitivity cannot be utilized without a new class of IR focal plane arrays whose performance matches that of the telescope. In particular, JWST focal planes must be able to withstand the ionizing-particle radiation environment expected for its Lagrange-point (L2) orbit and ten-year mission lifetime goal. To help determine their suitability for JWST, NASA is evaluating prototype megapixel-class readouts and hybrid detector arrays under proton bombardment to simulate the anticipated JWST lifetime radiation dose. This report describes the results of early tests on devices from two manufacturers using photovoltaic (HgCdTe or InSb) candidate near-infrared detector structures. Results to date have shown encouraging performance, along with some areas of continuing concern.

## 1. INTRODUCTION

We describe here characterization tests performed on two prototype candidate infrared detector focal plane arrays (FPAs) for JWST's near-infrared (NIR) instruments, including the Near-Infrared Camera (NIRCAM) Near-Infrared Spectrometer (NIRSpec), and Fine-Guidance Sensor. Rockwell Science Center's H-1RG and Raytheon Vision System's SB291 are megapixel-class building blocks designed to be representative of the larger structures proposed for JWST. Both devices are optimized around JWST NIR requirements (Table 1), with design operating temperatures between 30K and 37K.

Orbiting the second Lagrange point 1.5 million km from earth, JWST will be exposed to a potentially damaging cosmic ray environment. Depending upon the level of shielding provided to the detector arrays in the final design, a lifetime dose of 5krad(Si) to 50krad(Si) is anticipated.

The SB291 (and its 2048X2048 counterpart, the SB304) draws on Raytheon's successful 'ALADDIN' and 'Orion' readout architectures<sup>1</sup>, applying refinements tailored for the near-IR application. The SB291 is essentially a 'quadrant' of the four-output SB304, and the readout is mated to an indium antimonide (InSb) detector substrate at a pixel pitch of 25 $\mu$ m. InSb detector material requires a 30K operating temperature for the SB291, compared to 37K for the H-1RG.

The H-1RG (and the H-2RG, its 2048X2048 version) is a hybrid device comprising a sophisticated software-configurable silicon readout circuit and a mercury-cadmium-telluride (HgCdTe) detector array optimized for the JWST NIR spectral range. The readout includes a serial port to allow user selection of various operating modes, including the number of parallel outputs and output stage amplifier configuration. Several clocking and reset modes are available, including 'guide mode' operation wherein a selectable subarray may be dedicated to a guide star and read out independently. Pixel read rates up to 5MHz are available.

Other groups<sup>2,3</sup> have characterized a wide range of performance metrics for these devices. Our laboratory test effort has been tightly focused on evaluating the performance degradation to be expected for JWST lifetime radiation dose levels. We have placed particular emphasis on dark current activation, a crucial determinant in meeting JWST's science goals.

In Section 2, we highlight the development program for these devices. Section 3 describes the devices under test in further detail. Section 4 describes the test program and equipment, and Section 5 summarizes the test results.

**Table 1.** *Relevant JWST NIR Detector Requirements.*<sup>4</sup>

Parameter	Requirement	Goal
Wavelength Range ( $\mu\text{m}$ )	0.6 - 5	0.6 - 5
Operating Temp. (K)	30 - 37	Highest possible
FPA Format	Multiple 2048 <sup>2</sup> SCAs	Multiple 2048 <sup>2</sup> SCAs
QE (%)	>70 - 80	> 90 - 95
Dark Current ( $e^-/s$ )	Fits noise budget	<0.01
Read Noise ( $e^-$ )	<9 (Fowler 8)	<2.5 (Fowler 8)
Well Capacity ( $e^-$ )	>60,000	>1E5
Power (mW/Mpixel)	$\sim$ 1	0.1

## 2.DEVELOPMENT PROGRAM

To understand the performance limitations imposed by the space radiation environment on the candidate near-IR JWST focal plane technologies, a program of testing and analysis was set up in conjunction with the Radiation Effects Working Group at the NASA Goddard Space Flight Center. The tested devices were produced through parallel NASA NIR focal plane development contracts at Rockwell Scientific (5- $\mu\text{m}$  cutoff HgCdTe) and at Raytheon Vision Systems (InSb), which ran from 1998 - 2003. Both contractors worked to demonstrate that JWST performance requirements could be met, and that the more ambitious performance goals could be approached. Among the performance challenges were achieving extremely low total noise (<10  $e^-$ ) over extended ( $\geq$ 1000 s) integration times, near-vanishing dark current levels, and high-performance anti-reflection coatings to cover the 0.6 to 5 $\mu\text{m}$  range.

The vendors developed both 1024 x 1024 and 2048 x 2048 element detector arrays and the associated two-dimensional multiplexers. Because in each case the architecture, processing steps, and detector geometries of the 1024<sup>2</sup> and 2048<sup>2</sup> devices were identical, the smaller-format devices were selected for testing convenience. Our lab was tasked with characterizing pre- and post-irradiation effects on the bare 1024<sup>2</sup> multiplexers (Rockwell H-1RG and Raytheon SB-291), and also the full hybrid arrays in five separate cyclotron tests. Testing was conducted at the vendor-selected optimum temperature within the allowable JWST range.

## 3.DESCRPTION OF DEVICES

### 3.1. Raytheon SB291 ROIC and InSb SCA

The 1024 x 1024-element SB291 readout multiplexer is a Source-Follower-per-Detector (SFD) design with three transistors per unit cell, formed in an epitaxially-grown layer on a Si substrate. Its architecture is similar to that of the proven CRC-206 'ALADDIN III',<sup>5</sup> but with a contiguous megapixel rather than independently-read quadrants. The SB291 uses a 25  $\mu\text{m}$  pixel, and input/output (I/O) pads on the SB291 are confined to one side so that the device is three-side buttable if used as the building block for a larger focal plane array. Four pixels in adjacent columns are addressed simultaneously with each valid pixel clock, yielding a column-interleaved output. A column of reference unit cells (identical to the other unit cells but with no detector attached) is added at either side of the readout, creating a 1032x1024 addressable area. The reference pixels serve to provide a 'black level' that may be used to subtract offset drifts in long-integration measurements. The device is a very close cousin to the SB270 'Orion' ROIC<sup>6</sup>.

To minimize power dissipation and possible glow while maintaining acceptable pixel SFD amplifier bandwidth, only two columns of unit cells are powered at a given time. Unit cell current is applied just before a given unit cell is

addressed in order to provide sufficient drive capability to slew the output bus during the address period. At any one time this 'slew' current source is applied to the unit cells being addressed and to the unit cells one address ahead. Thus only eight columns of pixels see the source-follower current at a given time. The design goal for readout rate was 600 kpixels/s total through four outputs, with a minimum unit cell address time of 6.7  $\mu$ s.

Both row-by-row and global reset modes are provided. There is no dedicated reset bias supplied to the unit cells. Instead, the reset switch shorts the integrating node to the drain of the integrating FET so detectors are reset to the drain potential plus an offset determined by charge redistribution associated with the opening of the reset and enable switches in the mux. Fowler sampling<sup>7</sup> was used in our tests to optimize read noise performance.

A number of lot splits were produced for this effort, with varied parameters including doping and thickness of the epitaxial layer. In the end, the vendor was asked to select the lot split to be evaluated under proton bombardment, and one ROIC from that lot split was selected for radiation testing. The ROIC was tested separately from the SCA to allow mux- and detector-related effects to be distinguished.

After candidates were evaluated in our laboratory a particular hybrid device was selected for proton bombardment to a dose of 5krad(Si). All the devices produced were engineering-grade prototypes, and as such had a number of cosmetic and functional defects. Of the SCAs whose ROIC substrate came from the same lot split as that selected for the bare ROIC test, the part deemed least likely to produce excess dark current from these defects was selected for the proton test.

### **3.2. Rockwell H-1RG ROIC and HgCdTe SCA**

The HAWAII-1RG readout multiplexer is also an SFD design, with an addressable area of 1024x1024 including a four-pixel-wide border of reference pixels, which are mixed in with the data stream by default. Each of two parallel outputs reads out a contiguous 512 columns (including reference pixels). Global reset mode is the default, and the H-1RG does incorporate a dedicated line to carry the reset potential to all unit cells. Input and output lines are confined to one edge of the device to make it three-side buttable as part of a larger focal plane array.

The readout contains a sophisticated array of built-in functions controlled via a set of registers that can be set 'on the fly'. Two of the clock input lines can be assigned to serve as a serial port connection to allow access to these registers, or the device can be run in a simple 'default' mode that is comparable in complexity and function to the SB291. For simplicity and to maintain this comparability, all our tests ignored the enhanced functionality of the H-1RG, and the description here refers only to the default configuration.

As with the SB291, a bare H-1RG ROIC was tested separately from the SCA to distinguish mux- and detector-related effects, and Fowler sampling was employed to improve read noise performance. Rockwell selected for test a H-1RG mux and SCA, along with a H-2RG SCA for which our test system could only digitize two discontinuous 512x1024 subarrays. The H-1RG SCA was tested to 50krad(Si), and the H-2RG to 5krad(Si).

## **4. TEST PROGRAM**

### **4.1. JWST detector performance requirements**

As described in JWST document 570<sup>8</sup>, the radiation environment anticipated for the JWST mission is comprised largely of energetic cosmic-ray protons. Long-term performance degradation in the ROIC related to total absorbed dose is thought to be caused largely by trapping of strongly ionized charge under oxide layers in the multiplexer, leading to a long-term offset shift in the operating point of affected transistors. These changes can lead to changes in power dissipation and linearity of the multiplexer, and can render it inoperable at sufficiently high dose levels.

Displacement damage is believed to be the predominant mechanism in the detector substrate, leading to increased dark current in affected pixels. During JWST's mission lifetime a fraction of the detector array will be degraded to the point where it no longer meets the read noise requirement due to radiation-activated dark current. This damage can be annealed to some extent, but at JWST operating temperatures such damage is essentially permanent.

Table 2 presents a subset of the JWST NIR requirements matrix that is relevant to instrument radiation-environment performance. Transient radiation effects, such as charge from individual proton events and luminescence from irradiated surrounding materials, can have as great an effect on device performance as long-term device degradation.

**Table 2.** Radiation-related performance requirements for JWST NIR instruments<sup>9</sup>

Performance Parameter	NIR Channel
Total Noise	10 e <sup>-</sup> rms (3 e <sup>-</sup> rms goal for spectroscopy)
Operating Temperature	30 -37K
Pixel Pitch	15 $\mu$ m – 30 $\mu$ m square
Pass Band	0.6 $\mu$ m – 5 $\mu$ m
Radiation Immunity	'causes minimal effect'
Cosmic Ray Pixel Upsets	< 10% of pixels above noise req.
Maximum Exposure (On-Target Integration) Time	1000 seconds
Frame Time	12 seconds

#### 4.2. Transient effects

Of the various charged-particle interactions that can occur when protons pass through these detector arrays, our test effort was conceptually split into two areas of concern: cumulative 'total-dose' effects, and single-event-upsets (SEU). As part of our radiation test program for these devices, specialized tests were developed to focus on the short-term interaction of individual protons with the device under test (DUT). Detailed measurements of the time development of the transient signal, spreading of the ionized charge, and the effects of luminescence and secondary ionizing events were obtained. Analysis of the data collected in this phase of the test is beyond the scope of the present paper, and we defer detailed results of the SEU studies to a separate article<sup>9</sup>. The present paper deals only with effects related to total dose.

#### 4.3. Total dose effects

Radiation degradation can be mitigated through proper device design, and through optimized detector array processing at the semiconductor-wafer level. Thin layers and small feature sizes tend to be helpful in producing radiation-hard parts, but there are no hard-and-fast rules that can be applied to yield devices that are impervious to radiation damage. Thus it is necessary to determine empirically the level of radiation 'hardness' achieved in a particular design.

A number of performance factors may be influenced by the radiation-environment history of a device. The list includes detector dark current and optical response, multiplexer amplifier linearity and transistor threshold voltages. These factors tend to degrade overall device sensitivity due to increased read noise and decreased operability.

Of the various total-dose related performance factors, it is radiation-activated dark current that demands the most attention in these tests. This 'activation' of dark current is well-known in space-based infrared sensors, but due to the exceptional dark current performance exhibited by this latest generation of NIR detector arrays it has become quite difficult to accurately characterize. Baseline pre-irradiation dark currents are on the order of millielectrons per second, necessitating very long integrations in 'perfectly' dark cryostats to become measurable quantities. Data artifacts due to amplifier drifts, terrestrial cosmic ray effects, and (after irradiation) induced radioactivity in the cryostat must be accurately subtracted. Although a wide range of performance metrics were collected in the course of these tests, the preponderance of the results presented here deal with the issue of activated dark current.

#### 4.4. Test setup

Tests were conducted in our own laboratory at NASA Ames Research Center and at the Crocker Nuclear Laboratory (CNL), University of California at Davis. The 88-inch cyclotron at CNL has been used for a number of proton tests of prototype astronomical focal plane arrays, including those used in the two long-wavelength bands of the Infrared Array Camera instrument in the Space Infrared Telescope Facility (SIRTF)<sup>10</sup>. The cyclotron makes available protons of selectable energies up to 63MeV.

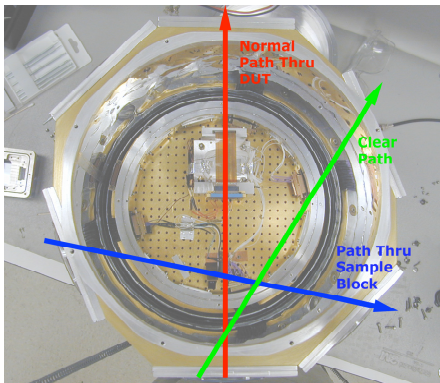


Figure 2. Top view of disassembled cryostat showing available proton paths.

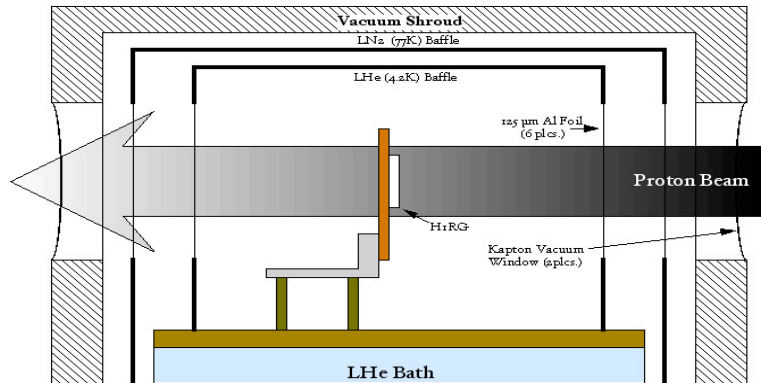


Figure 1. Schematic showing arrangement of normal beam to DUT.

In order to facilitate the range of proton interactions to be studied, we have constructed a cryostat that allows irradiation at varying angles of incidence through a set of six 'windows' (Figure 2). Each of the windows consists of a series of 100mm diameter ports cut in the vacuum shroud and internal radiation baffles to allow nearly free transport of protons through the cryostat, with only the device under test providing a significant obstruction. Thin Al foils offer a minimum of shielding while maintaining a dark optical environment even where the internal baffles have been cut away. Low-Z (Kapton) windows are employed at the outer housing to maintain cryostat vacuum (Figure 1). Every effort has been made to 'stop' the minimum amount of proton energy in the cryostat, so as to mitigate the influence of induced radioactivity in the test data. Despite these efforts, a fair amount of energy is inevitably deposited in the materials used by the vendors in mounting and packaging the test devices and the resulting artifacts complicate data analysis significantly.

The cryostat was aligned at the end of the cyclotron beam line with the aid of fiducial lasers. Alignment was verified through exposure of photographic film placed at the cryostat exit window, ensuring that the proton beam was passing through the intended path. Beam density profiles were obtained prior to the beginning of our test series to verify the uniformity of proton flux across the diameter of the exit window.

Data acquisition was through our laboratory test system, repackaged for transport and use at UCD. This test system consists of clocking and digitizing boards in a VME chassis, interfaced to a Macintosh host computer running a custom LabView user interface. This data system has been described elsewhere<sup>11</sup>, and its reliability has been established over years of use in our laboratory.

## 5.RESULTS

### 5.1. Pre-radiation-test characterization

#### 5.1.1. Dark current

Prior to irradiation dark current was measured through a succession of long integrations of increasing period, up to 3500s. In Figure 3 we show results of a typical dark current series obtained for the Raytheon SB291 at a temperature of 30K. In Figure 3, the Fowler-4 signal of the median operable pixel is plotted along with that of the median reference pixel. Subtraction of the reference signal provides a first-order correction for drifts and integration-time-dependent offsets, giving a more accurate

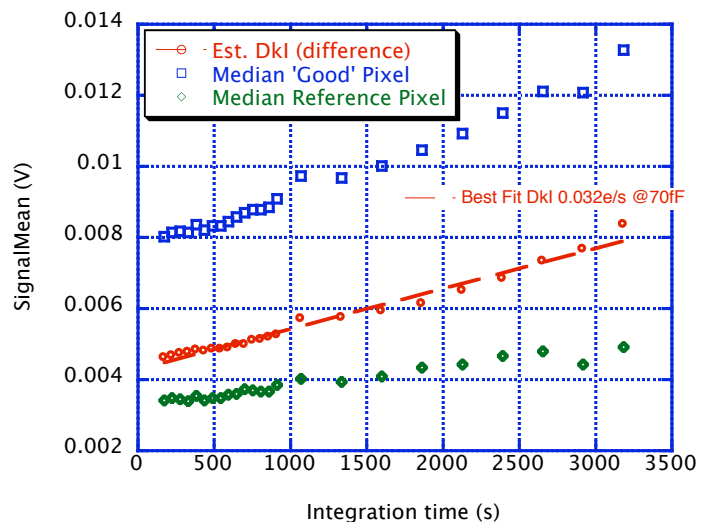


Figure 3. SB291 dark signal v. integration time

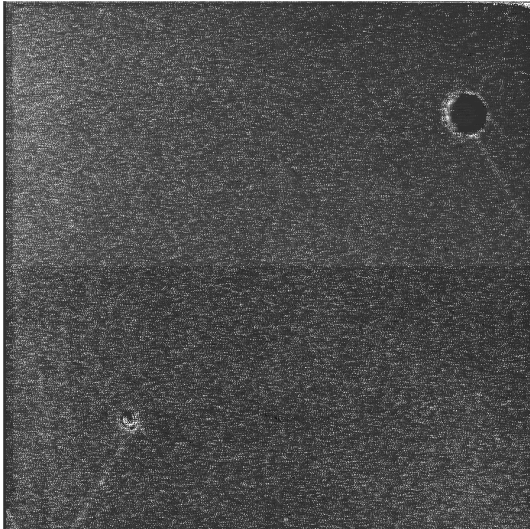


Figure 5. Pre-irradiation SB291 Dark Current map.

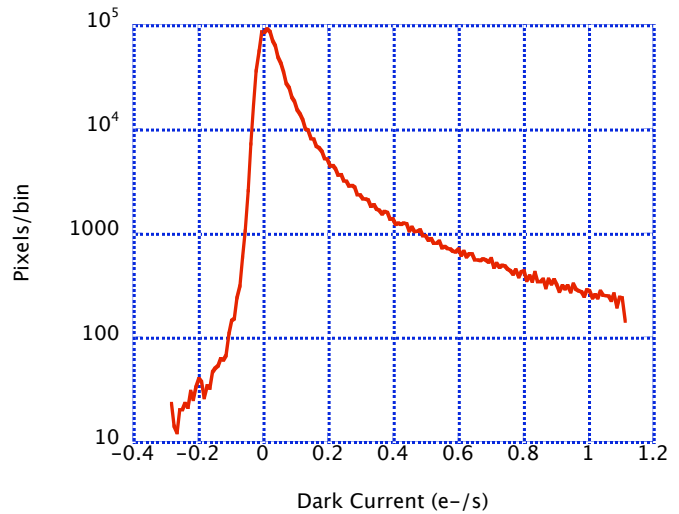


Figure 4. SB291 dark current distribution based on difference of 2126s and 542s dark frames. Effective bias=300mV. Bin width=.008e/s.  $C_{in}=70fF$ ,  $G_{sf}/n=0.78$ . No reference pixel subtraction.  $T=30K$ .

indication of detector dark current. Equivalent plots for the H-2RG parts are similar.

Each manufacturer supplied an 'Engineering-grade' device for the potentially destructive radiation test. As such, these devices displayed a number of cosmetic defects and 'hot' pixels, and thus did not meet the stringent JWST flight FPA operability requirements going into our test. Figure 5 and Figure 4 display a spatial map and a distribution of pixel dark currents for the SB291 device, while Figure 6 and Figure 7 display equivalent information for the H-2RG device (note that we are clocking a non-contiguous 1024x1024 subarray of the H-2RG, accounting for the apparent spatial discontinuities). Reference pixel corrections have not been applied in these plots.

The significant number of defective pixels in each test device presents a challenge in characterizing dark current and its subsequent radiation activation. Some of the 'hot' pixels in a given frame are cosmic-ray artifacts, and read noise will cause a further fraction to occasionally exceed a given dark current threshold in a particular measurement. On the assumption that flight parts will have very few marginal or defective pixels, our primary interest is in the radiation-

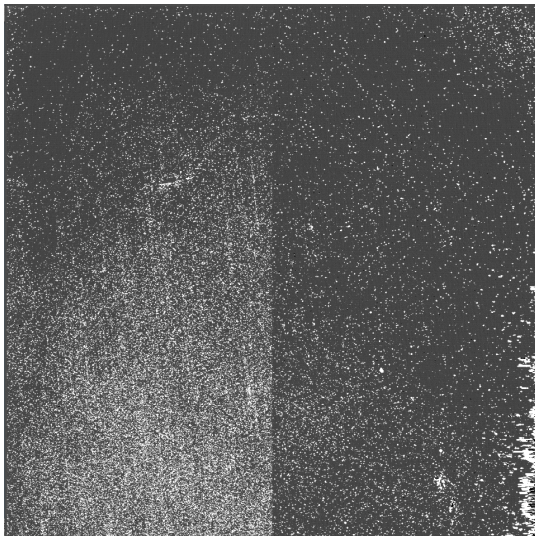


Figure 6. Pre-irradiation H-2RG Dark Current map. showing the 1024x1024 subarray examined in our SCA radiation tests.

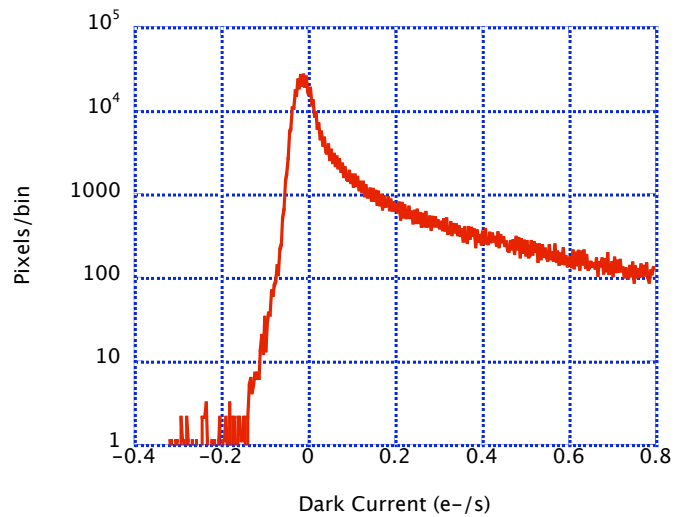


Figure 7. H-2RG dark current distribution based on difference of 1400s and 100s dark frames. Bin width=.003e/s  $C_{in}=50fF$ ,  $G_{sf}=0.98$ . No reference pixel correction.  $T=37K$ .

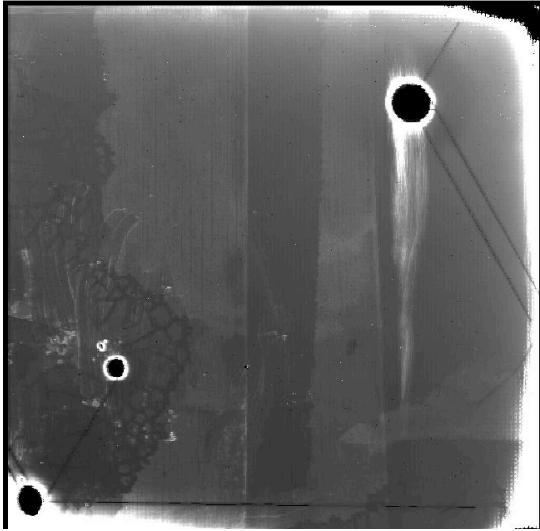


Figure 9. SB291 response to IR stimulator. White level set to maximum pixel response.



Figure 8. H-IRG response to IR stimulator. White level set to maximum pixel response.

hardness of the pixels that meet the JWST flight spec. A strategy developed to isolate test article engineering defects is described in a post-rad-test results section below.

### 5.1.2. Response

Geometry in the test cryostat compromised our ability to deliver a uniform and well-calibrated illumination to the device under test, in favor of optimizing proton transmission paths and minimizing induced radioactivity in the cryostat. A simple nichrome stimulator was employed to give an uncalibrated flood illumination at the position of the test article. A fixed voltage applied to the stimulator served as the reference illumination level, subject to the inherent stability of the source over the duration of the test series. The stimulator was not directly irradiated by the proton beam, but probably absorbed some secondary radiation which may have affected its output. No significant evidence of radiation-induced change in stimulator output was observed. Figure 9 and Figure 8 show representative response maps of the test SCAs, showing clearly the degree of cosmetic and operability imperfections present in these engineering devices.

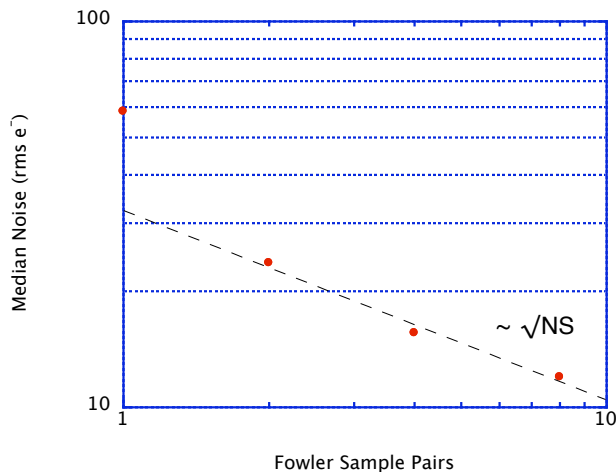


Figure 10. SB291 Read noise v. Fowler pairs.  $T = 30K$ . Electron conversion based on  $C=70fF$   $G_{sf}=0.78$ .

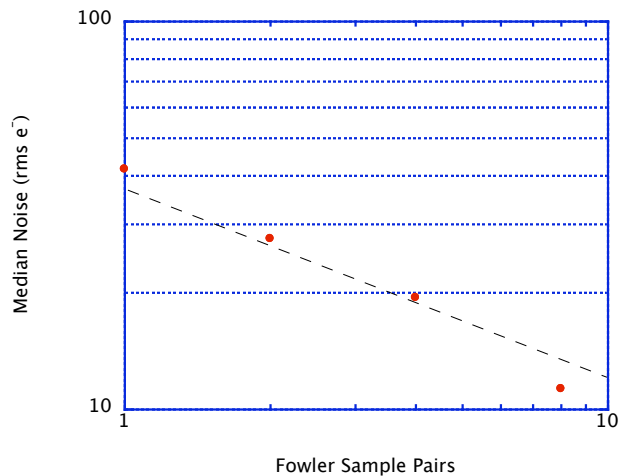


Figure 11. H-2RG Read noise v. Fowler Pairs.  $T = 37K$ . Electron conversion based on  $C=50fF$  and  $G_{sf}=0.98$ .

### 5.1.3. Read noise

Read noise was characterized as a function of number of Fowler-sample pairs at nominal JWST-proposed operating temperature (30K for Raytheon InSb, 37K for Rockwell HgCdTe). Time constraints did not allow detailed optimization of noise performance, which nonetheless was on par with expected performance based on measurements elsewhere.

As shown for each device in Figures 10 and 11, read noise varies roughly with the square-root of the number of Fowler sample pairs employed, as expected, up to at least 8 Fowler pairs. At 8 Fowler pairs, the SB291 reaches 11 rms electrons in our test system, and the H-2RG is close to 10 rms electrons.

## 5.2. Post-radiation performance

### 5.2.1. Dark current activation

Of the various figures of merit examined in these test, dark current activation is the most difficult to accurately characterize. It is also the most crucial parameter in determining the ability of the device to preserve the sensitivity necessary to reach JWST NIR science goals, since dark current is likely to set the ultimate sensitivity of the system.

Due to the large fraction of pixels not meeting spec in these 'engineering-grade' devices as delivered, these parts obviously could not be certified as meeting the JWST spec after radiation testing. A decision was taken to concentrate on the best subpopulation of each device, on the presumption that 'science-grade' devices from each manufacturer will include very few defective pixels. As described in Section 5.1.1 above, at these dark current levels the number of 'good' pixels is difficult to precisely quantify in the presence of read noise, cosmic-ray events and induced radioactivity in the cryostat.

In order to isolate and remove engineering defects from the test data, another long series of darks was obtained in a clear environment with each test SCA prior to the radiation test. The distribution of dark currents estimated from the longest integration for each SCA was examined to determine the width of the peak in the histogram and thus the accuracy to which we can estimate dark current in these devices. This distribution width arises from a combination of system read noise and of the true non-uniformity in dark current among the best pixels in the device. From the observed distributions it appears that read noise is the greatest contributor to this width for each test SCA.

We chose to set a dark current threshold for each long-integration frame in the dark current series at the median-pixel dark current plus the distribution width of the longest integration frame, as given by its full-width-half-maximum. This method allows us to quantify the 'hot' dark current pixel count with a number that is essentially independent of the fluctuations pixel signal as a function of integration time seen in Figure 3. By applying this threshold in each of the long-integration frames and removing from our select population any pixel that exceed the threshold in any of the frames, we develop a subpopulation of pixels that never exceed the dark current threshold over many hours of data collection. Post-irradiation data reduction is limited to this very conservative subpopulation of selected pixels.

This method is guaranteed to misidentify a number of good pixels as bad, since it makes no attempt to correct for the effects of cosmic ray events that occur during the long integration series, and because read noise will occasionally push marginally good pixels above the threshold. We are happy to give up these good pixels, since we are not trying to identify the absolute number of good pixels present before and after irradiation, just the percentage affected. The selected subpopulation comprises 63% of the SB291's pixels, and 54% of the H-2RG's.

After 5krad(Si) total proton irradiation and an extended period to allow decay of induced cryostat radioactivity (throughout which the nominal operating temperature was maintained), the series of long dark integrations was repeated in our lab to determine the number of pixels lost from the select subpopulation due to radiation-induced dark current activation. Dark current distributions estimated from the longest post-irradiation frame (and limited to the pre-radiation-identified select subpopulation) are given in Figure 12. The post-radiation distribution shows an extended tail toward higher dark current values in each case. The slight median shift in the H-2RG histogram is a test artifact that might be removed by reference pixel subtraction, which we have chosen not to perform here. We emphasize that each pixel in these distributions passed the stringent dark current thresholding described above in each of the pre-test dark current frames, and those that now appear in the high-leakage tail are either exhibiting radiation-induced dark current activation, or represent an ionizing event due to cosmic or residual activation in the cryostat following the decay period.

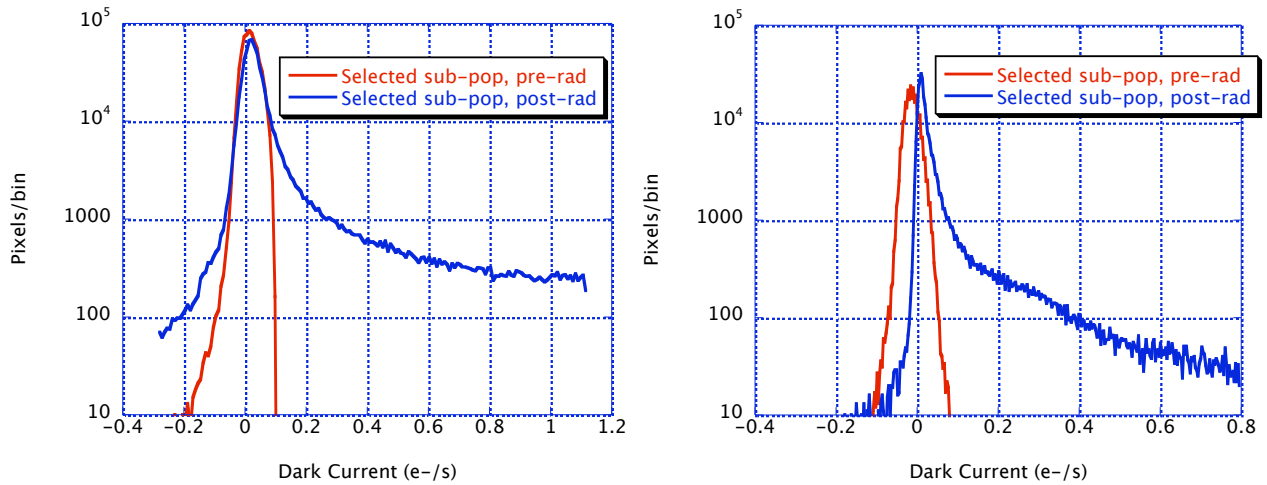


Figure 12. SB291 (left) and H-2RG good subpopulation dark current distributions, before and after 5krad(Si) proton irradiation.

We distinguish ionizing events from activated dark current pixels by a process similar to that used to select the good subpopulation in the pre-rad data. A threshold derived from the distribution width obtained from the pre-rad data is used on the post-rad distributions to flag hot pixels in each of the post-rad long dark frames, and a per-pixel count is performed to give the number of measurements in which a given pixel exceeds the dark current threshold so set.

A distribution of this per-pixel count is given for each device in Figure 13. We are more reluctant to mis-classify pixels as 'hot' in the post rad data than we were in the pre-rad data, as misclassification in the post-rad data will skew the percentage of pixels we identify as activated. We chose to examine the data using a range of threshold values derived from the pre-radiation distribution width for each device, using even multiples of the equivalent pre-rad standard deviation of dark currents. For each chosen threshold value we generated a 'hot-flagged' histogram (as shown for 4 $\sigma$  and 8 $\sigma$  in Figure 13). We chose to count as 'hot' the total number of pixels in the top three bins of the histogram. Thus to be counted as activated in our test a given pixel had to fall below a very tight threshold every time it was measured before the radiation exposure, then exceed a larger threshold value at least 11 times out of 13 measurements after the radiation exposure. A combination of read noise, cosmic ray events, and residual radioactivity in the cryostat is deemed unlikely to cause a pixel to be flagged as hot 11 out of 13 times, and we interpret this value as the best estimate of dark current activation. Of the many different approaches we tried in interpreting these data, we feel this method gives the most useful result.

In Table 3 we show the percentage of the initial good subpopulation determined to be activated following 5krad(Si), for various settings of the dark current threshold value. The number identified does not depend very strongly on how many of the top bins we include in the hot count or on the setting of the threshold. We have chosen to characterize the hot pixel count based on the 6 $\sigma$  threshold value. At this threshold the SB291 has lost 8% of the initial good subpopulation, while the H-2RG lost 10%. It should be noted that our test of the H-2RG dosed the device unevenly, with 5krad(Si) applied to a 512x1024 subarray, with the other 512 columns receiving only 2krad(Si). We consider only the higher-dosed columns here, accounting for the smaller initial population for the H-2RG. Additionally, a correction was applied for the Raytheon array to account for 'echoes' present in the data stream due to insufficient current (and thus insufficient slew rate) in the output driver during the test, that led to double-counting of some hot pixels.

Table 3. Activated dark current after 5krad(Si).

	Raytheon SB291	Rockwell H-2RG
Selected Starting Pixels	663497 (63%)	278323 (54%)
Ending Degraded Pixels	2 $\sigma$ : 87461 (13%)	2 $\sigma$ : 35799 (13%)
	4 $\sigma$ : 61913 (9%)	4 $\sigma$ : 30234 (11%)
→	6 $\sigma$ : 51428 (8%)	6 $\sigma$ : 26822 (10%)
	8 $\sigma$ : 45854 (7%)	8 $\sigma$ : 24395 (9%)

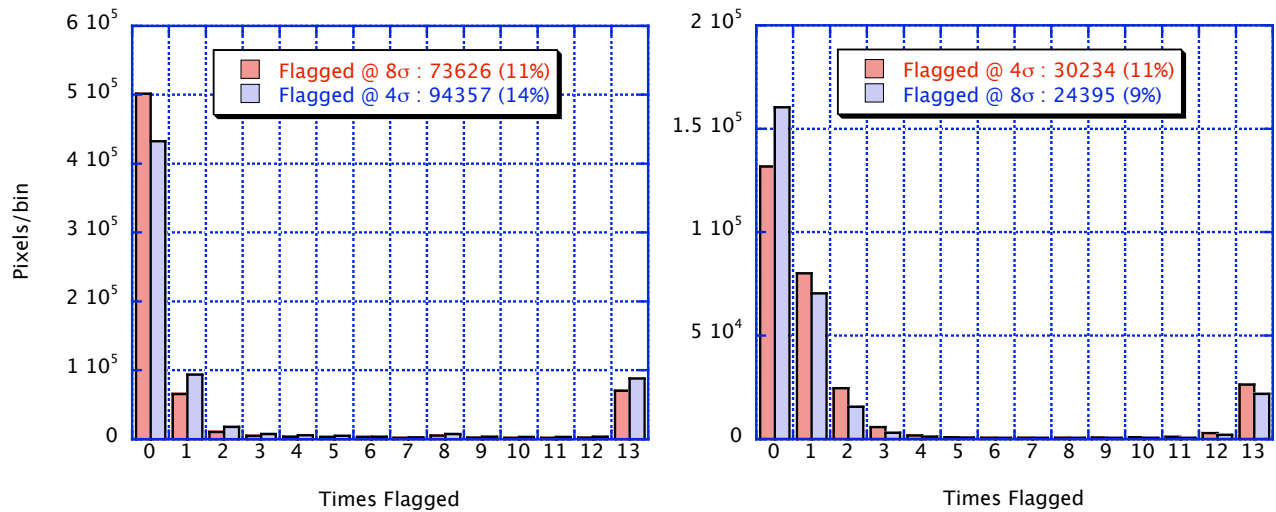


Figure 13. 'Hot-flagged' histograms for SB291 (left) and H-2RG over a long series of dark frames following 5krad(Si) and an extended 'cooling off' period at operating temperature to allow induced radioactivity in the cryostat to subside..

### 5.2.2. Responsivity shift

Figure 14 gives a comparison of response histograms for each part, showing the pre- and post-irradiation distributions overlaid to give an idea of the measured variation in response following the radiation test. It is worth pointing out that the stimulator used is uncalibrated and non-uniform, and that it illuminates the devices differently due to variation between the mounting geometry for the two parts. In each case there was an observed decrease in response on the order of a few percent. Whether this decrease is physically significant, given the crudeness of the optical arrangement, is not clear. If real, this loss in response would not significantly compromise the ability of JWST to meet NIR science goals.

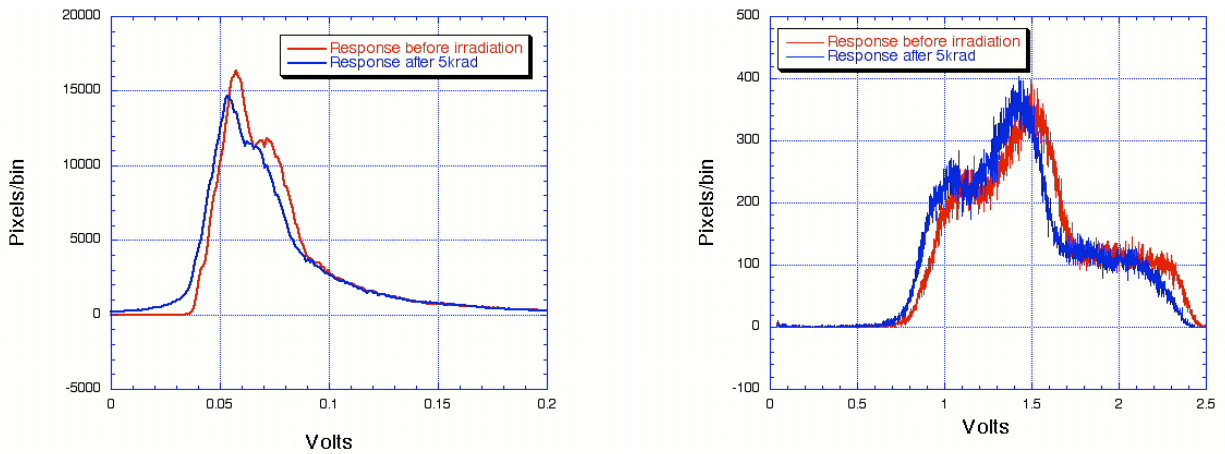


Figure 14. SB291 and H-2RG response variation following 5krad(Si) irradiation.

Similarly, there were no significant changes observed in read noise, amplifier linearity, or power dissipation after a dose of 5krad(Si) for either SCA. These latter parameters are largely dependent on readout operation, which was not as significantly affected by the 5krad(Si) dose.

### 5.2.3. FET Offset Shifts

During ROIC testing measurements were made of the source-follower output voltage as a function of dose, up to levels as high as 50krad(Si). These measurements are an indication of the true radiation hardness of the multiplexer, independent of detector effects. Figure 15 shows a comparison of FET threshold shifts, as indicated by changes in the source-follower output voltage, as a function of cumulative dose.

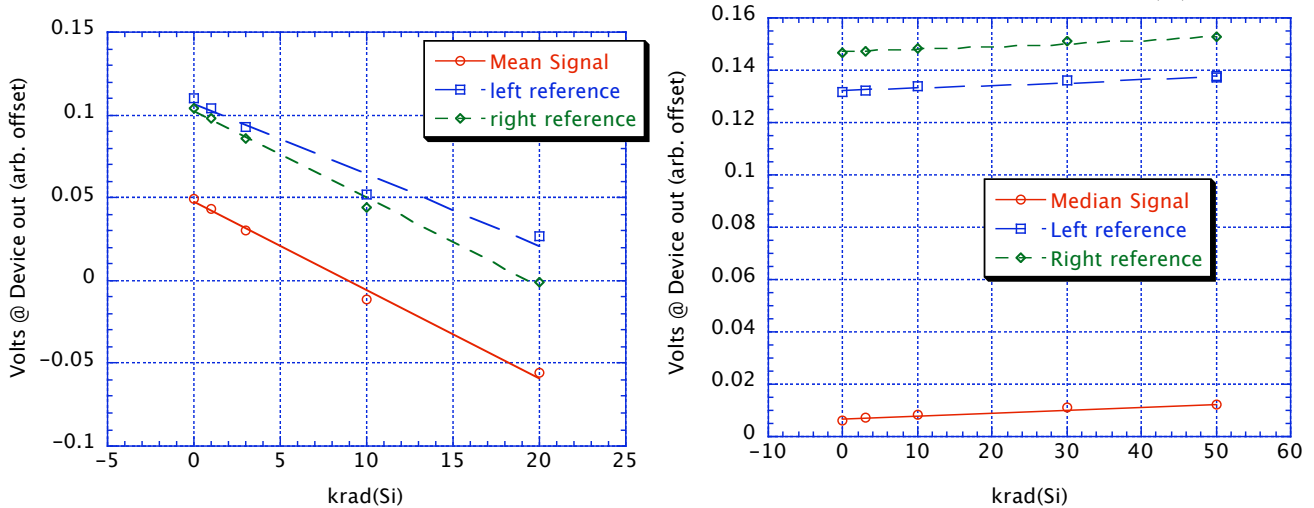


Figure 15. Observed shift in output voltage as a function of cumulative dose for SB291 (left) and H-1RG ROICs.

It is clear from Figure 15 that the Rockwell ROIC is inherently more radiation-hard than the Raytheon readout. The Rockwell readout showed essentially no radiation damage up to 50krad(Si), changing its output voltage by only a few mV. The Raytheon readout stopped working between 20krad(Si) and 30krad(Si), and showed an essentially linear output shift of about 5mV/krad(Si). The anticipated shift in the Raytheon array over the life of the NIRCAM mission would represent a significant fraction of the bias voltage applied to the InSb detectors, and would likely require adjustment of applied biases to maintain performance levels. Due to the limited duration and funding of the JWST development program, Raytheon was not able to provide a more rad-hard mux design for these tests.

Bare ROIC tests showed that both devices met the JWST NIR instrument 5krad(Si) radiation-hardness requirement, but the extra margin built into the Rockwell ROICs might prove useful in the event of higher-than-anticipated lifetime dose levels.

## 6.SUMMARY

The test results presented here describe data collected over the course of independent irradiations of ROICs and SCAs from two manufacturers in competition to produce the flight focal plane arrays for JWST's NIR instruments. Both manufacturers provided devices performing at a high level, encouraging the hope that most (if not all) of JWST's NIR science requirements are very nearly within the reach of today's technology. Our approach was to closely examine radiation hardness, performing nearly identical tests in a clear laboratory environment and in a proton environment provided by a cyclotron, taking as great an advantage as possible of our opportunities to gather a deeper understanding of the test devices in extended laboratory tests.

The proton environment was chosen to simulate to the best of our ability the on-orbit radiation environment anticipated for JWST. Terrestrial simulations can never exactly duplicate space environments, but we believe this test data provides a useful evaluation of expected radiation-hardness of these two candidates. Single-event data, to be presented elsewhere, was obtained to characterize the real-time effects of radiation on the data stream, and to evaluate different strategies for mitigating its effect. Total-dose effects, described here, were also examined to characterize the ability of these devices to continue to deliver high levels of sensitivity throughout the mission lifetime.

In the crucial criterion of dark current activation, both devices lost about 10% of pixels after 5krad(Si). This number was very conservatively measured, and under the data reduction algorithm used is not strongly dependent on settings of threshold levels over a reasonable range. This degree of dark current activation is within a factor of two of JWST NIR operability requirements, but the doses here were deposited over a very short period compared with the mission lifetime and spontaneous real-time annealing of radiation damage during the mission might make the difference between meeting the requirement and missing it.

Most other performance parameters were unchanged after 5krad(Si), but we observed a substantial difference in the inherent radiation hardness of the two ROICs, with the Rockwell readout showing an offset shift with dose that was more than 40 times less than that of the supplied Raytheon part.

Data obtained at dose levels above and below the 5krad(Si) requirement are presently being analyzed and may ultimately shed more light on ways this technology might be improved to better meet JWST NIR goals.

## 7.ACKNOWLEDGEMENTS

We wish to thank NASA's James Webb Space Telescope Project Office for supporting this work, and especially Dr. Carlos Castaneda and the staff of the Crocker Nuclear Laboratory at the University of California, Davis for their invaluable help with the tests.

## 8.REFERENCES

---

<sup>1</sup> K. M. Merrill et al., "Orion II: the second-generation readout multiplexer for largest infrared focal plane", Paper 1567-21, elsewhere in this conference.

<sup>2</sup> C. W. McMurtry et al., "James Webb Space Telescope: characterization of flight candidate NIR InSb array", Paper 1567-17, elsewhere in this conference.

<sup>3</sup> D. F. Figer et al., "Independent testing of JWST detector prototypes", Paper 1567-29, elsewhere in this conference

<sup>4</sup> C. McCreight, M. Greenhouse, D. Figer, R. Martineau, M. Jurotich, and B. Seery, "NGST ISIM Technology Development requirements and Goals for NGST Detectors", <http://www.ngst.nasa.gov/doclist/bytitle.html> Document 641 (2001)

<sup>5</sup> A. M. Fowler, I. Gatley, P. McIntyre, F. Vrba, A. W. Hoffman, "ALADDIN: the 1024x1024 InSb array—design, description, and results," SPIE **2816**, pp. 150-160 (1999)

<sup>6</sup> K. M. Merrill et al., "Orion II: the second-generation readout multiplexer for largest infrared focal plane", Paper 1567-21, elsewhere in this conference.

<sup>7</sup> Fowler, A.M. and Gatley, L., "Demonstration of an Algorithm for Read-Noise Reduction in Infrared Arrays," *Astrophys. J.* **353**: L3-4 (1990)

<sup>8</sup> J.L.Barth, J.C. Isaacs, and C.Poivey, "The Radiation Environment for the Next Generation Space Telescope," NGST Document 570, September 2000.

<sup>9</sup> J. Pickel, in preparation.

<sup>10</sup> R. McMurray, R.R. Johnson, C.R. McCreight, M.E. McKelvey, J.D. Garnett, A.W. Hoffman, N.A. Lum, W.Y. Lum, M.S. Smith, K.P. Sparkman, A.G. Toth, G. Domingo, D. Krebs, M. Jhabvala. "Si:As Array Performance for SIRTF/IRAC," SPIE. **4131**: pp. 62-69 (2000)

<sup>11</sup> W. I. Ogilvie, 'A Parallel DSP Data Acquisition System for Evaluating IR Detector Arrays', SPIE **4850**, pp. 971-980 (2003)